ACS APPLIED MATERIALS & INTERFACES

Article

Grafting commercial surfactants (Brij, CiEj) and PEG to electrodes via aryldiazonium salts.

Ophélie Squillace, Charles Esnault, Jean-François Pilard, and Guillaume Brotons

ACS Appl. Mater. Interfaces, **Just Accepted Manuscript** • DOI: 10.1021/acsami.7b12164 • Publication Date (Web): 10 Nov 2017

Just Accepted

ACS Publications

ACS Applied Materials & Interfaces is published by the American Chemical Society.
1155 Sixteenth Street N.W., Washington, DC 20036

Grafting Commercial Surfactants (Brij, CiEj) and PEG to Electrodes via Aryldiazonium Salts.

Ophélie Squillace, Charles Esnault, Jean-François Pilard and Guillaume Brotons.*

* Corresponding author E-mail: guillaume.brotons@univ-lemans.fr Tel: +33 243832625

IMMM, Institut des Molécules et Matériaux du Mans, Université du Maine - UFR Sciences et Techniques, Avenue Olivier Messiaen, 72085 Le Mans, France.

KEYWORDS. Surface functionalization; Aryldiazonium salts; Non-ionic diblock copolymer and oligomeric surfactants; Brij and CiEj surfactants; Thin films; Electrochemical impedance spectroscopy.

ABSTRACT. Grafting commercial surfactants appears to be a simple way to modify electrodes and conducting interfaces, avoiding the synthesis of complex organic molecules. A new surface functionalization route is presented to build surfactants coatings with monolayer thicknesses grafting molecules considered as non-reactive. A monolayer of $–SO_2Cl$ functions (from a para-benzene sulfonyl chloride) was first electro-grafted. It shown a high reactivity toward weak nucleophiles commonly found on surfactants end-moieties such as hydroxyl groups (-OH) and it was used to covalently graft: 1) non-ionic diblock oligomers (Brij or CiEj, $C_xH_{2x}+1(OCH_2CH_2)_nOH$ with x=16 and n=23 for Brij58; x=16 and n=10 for Brij C10; x=16 and n=2 for Brij52); 2) Poly (ethylene glycol) PEG short chains (PEO_9 for $(OCH_2CH_2)_nOH$ with n=9); and mixed formula. The surface modification due to these molecular coatings was investigated in terms of wetting properties and interfacial electrochemistry characteristics (charge transfer resistivity, capacity and ions dynamics). Built on flat and transparent thin chromium films, Brij and PEO mixed coatings prove to be promising coatings for electrochemical biosensor application such as for stabilizing a partially tethered supported biomimetic membranes (tBLM).

Introduction

Polymer brushes and smaller oligomer chains, grafted to a surface [1] represent an important class of coatings in bio-technologies. Chemisorbed chains, that are grafted to the surface via a covalent anchor, are much more resistant than physisorbed ones. Such organic layers are of particular interest on ultra-flat electrodes with a roughness of few angstroms, such as metal thin films that stimulate a strong interest for different applications. For sensors applications and for biochips used in day-to-day bio-analytical chemistry assays, the immobilization of a molecule on a surface (so-called the "ligand") is a prerequisite step to test its affinity with a free partner in solution (so called the "analyte"). Several routine techniques, such as SPR (Surface Plasmon Resonance [2-3]), QCM (Quartz Crystal Microbalance [4-6]),... , also require a robust knowledge of the interactions with the functionalized metal film interface. For such experiments, the only way to relate unambiguously the sensor signal to the interface molecular organisation, is to keep its roughness as small as possible, much below the molecules dimension, in order to implement surface sensitive characterisation techniques[7]. With standardly used hand polished electrodes and "optical quality" electrode coatings, the roughnesses often reach tens of nanometers which is too high to allow the use of surface scattering techniques to probe the molecular organisation, such as x-ray and neutron reflectometry, AFM (Atomic Force Microscopy), surface sensitive microscopy (SEEC [8]), etc. Ultra-flat electrodes are thus needed and can be elaborated as thin metal films deposited on floated glass microscopy slides, silicon wafers, soft-polished sapphire blocs or cleaved mica sheets, up to a cm² while keeping a low top roughness and sufficient electron conductivity. For noble metal electrodes such as gold, the formation of organic self-assembled monolayers (SAMs) using alkanethiolates was extensively investigated [9-10]. More particularly, commercially available alkane thiols with 10 to 18 carbon atoms self-assemble in few minutes to form air stable monolayers. Such molecules can further graft on specific molecules of interest (proteins, viruses, etc…) through their –COOH or -NH_2 ending moieties. In this process, strong hydrophobic molecular interactions are the key point to form the SAM and to obtain higher coverage densities. Nevertheless, SAMs also affect the electrode capacity and might hinder charge transfer. Moreover, thiols on noble metals appears to form relatively weak covalent linkers that do not always withstand the electric fields needed in aqueous solutions[11]. The decomposition of aryldiazonium salts with the electrode offers an attractive alternative to obtain a more robust linker. Electrografting by the reduction of aryldiazonium salt leads to aryl radicals that form a strong covalent bond with the electrode (1 electron mechanism Figure 1 a). This methodology can be applied to various conductors and semi-conductors, including in aqueous solutions. Since the pioneering work of Pinson and Savéant[12], the grafting method from the reduction of aryldiazonium salt was developed for a large variety of chemical groups [12-14]. This process is robust [15-16] and has been well studied and reproduced on metal electrodes [17-20]. The possibility to obtain a stable and highly organized organic monolayer or multilayer at the electrode surface was demonstrated from different grafting strategies [21-24].

To realise a stable covalent link between an electrode and unmodified surfactants, such as Brij/CiEj/... molecules, it is required to work on the nucleophilic -OH terminal group. We thus

chose the coupling reactant -SO_2Cl due to its high reactivity towards weak nucleophilic groups. Herein, the sulfanilic acid was used as a starting component for the formation of the organic layer where the -SO_3H group in para position will be further transformed in a sulfonyl chloride group [25]. It offers a good reactivity with chemical groups notoriously known to be weak nucleophiles (such as -OH,...) but that are often found as terminal groups of surfactants. In this respect, a large variety of surface coatings can be obtained avoiding the use of molecules selected for their highly reactive anchor group and that are often far from trivial to synthesise. The "grafting from" alternative that requires surface initiated polymerization (SIP) is particularly difficult for building controlled amphiphilic surface coatings and it requires rather reactive anchor groups that often forbid the presence of many functional groups and coupling agents.

This paper focuses on the "grafting to" method of amphiphilic diblock oligomers using their hydroxyl end-moiety (-OH, Figure 1 a). We tested this electrode functionalization, with a broad class of commercial non-ionic surfactants, namely Brij and CiEj, expected to change the surface properties depending on their hydrophilic/hydrophobic moieties lengths. Polyoxyethylene glycol alkyl ethers (Brij or CiEj, $CH_3–(CH_2)_{2–18}–(O-C_2H_4)_{1–25}–OH$) are among the most used non-ionic surfactants and their hydrophilic moiety (oligo-ethylene glycol, PEG methyl ether) is one of the most efficient water swelling group and brings non-fouling properties [26]. For this reason, we also studied how to graft PEO small chains (PEG , Poly ethylene glycol), through their hydroxyl moiety, and how to form mixed layers of Brij surfactants and PEO chains. In this way, we also avoid complex chemistry steps dedicated to add a reactive group to a PEG molecule [27]. Ultra-flat electrodes functionalized with Brij/CiEj and PEO mixed coatings are perfect environments for membrane electrochemical biosensors, where a single tethered bilayer lipid membrane (tBLM) is stabilized from anchor-harpoon molecules (here spare Brijs) on a PEO hydrophilic cushion [28-31]. Other applications are possible taking advantage of the amphiphilic nature of all the surfactants that can be grafted and using mixtures of them [32-34].

Experimental Section

Chemicals and Materials. Ethanol (EtOH, 99.8%), acetone (99.5 %), dichloromethane (99.9%), acetonitril (99.8%), methanol (99.7%), hydrochloric acid (HCl, 37%), sodium nitrite ($NaNO_2$), sulfanilic acid, $Fe(CN)_6^{3-/4-}$ redox couple, Brij58: ($C_{16}H_{33}(OCH_2CH_2)_{20}OH$), Brij52 ($C_{16}H_{33}(OCH_2CH_2)_2OH$), Brij C10 ($C_{16}H_{33}(OCH_2CH_2)_{10}OH$), PEO_9-CH_3 ($H(OCH_2)_9CH_3$), PEO_{23}-OH ($H(OCH_2)_{23}OH$) were purchased from Sigma–Aldrich (St Quentin Fallavier, France) and used without further purification. Milli-Q water (Versol, Aguettant, Lyon, France) were used.

Electrodes elaboration and cleaning. Three types of working electrodes were functionalized: 1) hand polished gold standard electrodes from Biologics™ with an apparent radius of 0.15cm (electrode area S_{WE}=0.07 cm²) ; 2) commercial gold coated quartz for microbalance experiments (from Biologics™, optical quality sensors). The gold thin film covers a cylindrical patch of 0.25cm radius (S_{WE}=0.196 cm² and σ_{RMS} = 1.2 nm). A specific cleaning protocol was established prior to using the QCM gold sensors since we observed a

high dispersion of the EIS data measured when sensors were used as received (see supporting materials, *Gold electrodes cleaning procedure,* Figure S-1) ; 3) Chromium thin films of 8 to 30 nm thick, evaporated on microscopy cover glasses (thickness ~170 μm and optical index ~1.5 from Cole-Palmer^{TM}) with a functionalized area S_{WE}=2.25cm² defined from the electrochemical cell geometry and a roughnesses $\sigma_{RMS} \leq 0.6$ nm.

Flat and transparent chromium electrodes. Chromium thin films of 20nm thickness (Cr, Neyco, 99.99% purity) were thermally evaporated on microscopy glass slides that were cleaned before in a mixture of methanol and hydrochloric acid (1:1), rinsed with purified water, dried and stored in dry atmosphere. The glass substrates were horizontally fixed in a Plassys ME300 metal evaporator that was operated at 10^{-7} mbar. A quartz crystal microbalance monitored the metal evaporation rate (0.1 nm/s) and the thickness during deposition. Atomic force microscopy (AFM) and x-ray reflectivity measurements (XRR), presented in the supporting materials were used to determine the density profiles of the films and top root-mean square roughness that was always below 0.6 nm. The best fits to the specular XRR data (Figure S-7) show a clear chromium layer with a dense core reaching the expected electron density ($\rho_{e,Cr}$ ~ 1.98 Å^{-3}), a diffuse interface of chromium with glass over 1nm ensuring a strong adhesion of the film and a Gaussian roughness at the air interface that also includes traces of stable oxidized phases (Cr_2O_3). Sputtered thin chromium layers were also deposited on thick glass in order to analyse their atomic composition using x-ray photoelectron spectrometry (XPS) with a mild ionic abrasion argon jet (XPS data shown in Figure S9 of the supporting materials, *X-ray photoelectron spectrometry*). XPS data confirmed the presence of chromium metal core with presence of thermodynamically expected oxide species at the two interfaces with substrate and air. The surface electric conductivity of the thin chromium films (~30nm thick layer) were measured using the four-terminal sensing technique. The values are consistent with the ones reported in the literature (σ~0.5.10^3 Ω^{-1}cm^{-1} [35-36]) with some dispersion since it is highly sensitive to the preparation method used. Conductivity increased by a factor of 10 by using sputtering deposition instead of chromium evaporation, which is useful in order to reduce the metal layer thickness (σ~0.3.10^4 Ω^{-1}cm^{-1} for 12nm sputtered film). This is a way to increase its optical transparency (Figure 1 c) so that optical microscopy through the glass substrate is possible (for imaging or fluorescence techniques). The paper focuses on the surface functionalization route and on the electrodes functionalities that can be obtained.

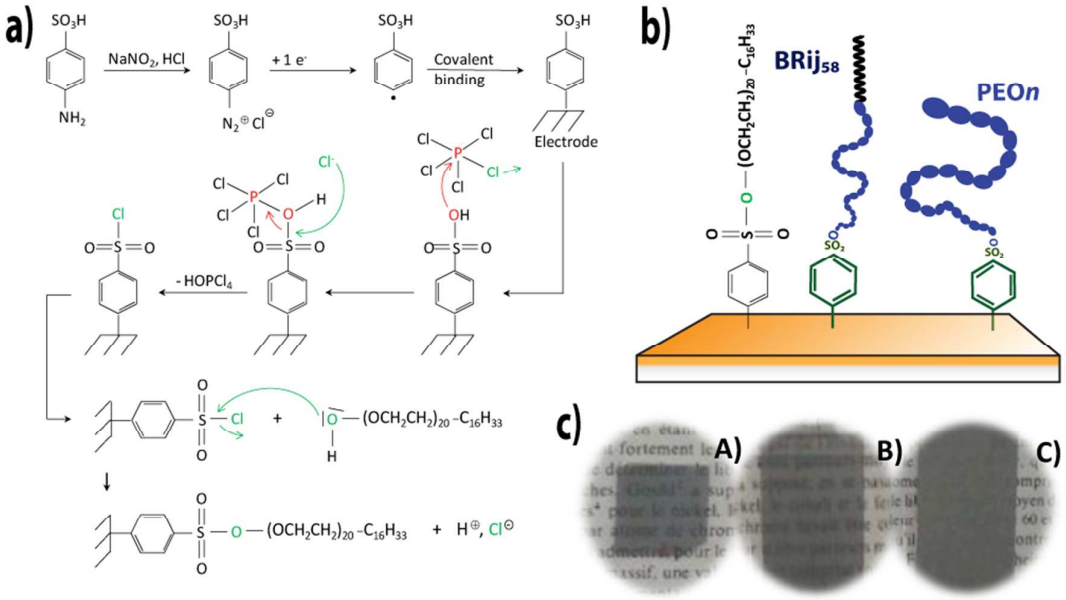

Figure 1. a) Scheme of the electrodes functionalization method involving commercial surfactants (here on the hydroxyl moiety of a Briji58 non-ionic amphiphilic diblock oligomer). The first two lines correspond to the "pre-functionalization" step (ending with –Ar-SO_2Cl) and next steps correspond to the "functionalization" (with surfactant or PEO grafting); b) Scheme of graft Brij58 and PEO ; c) Photographs of chromium coated microscopy slides, showing their transparency as a function of the deposited metal film thickness (8 nm Cr for A), 18 nm for B) and 28 nm for C))

Surface functionalization for grafting –OH terminated surfactants on electrodes.

In order to covalently graft the hydroxyl moiety of commercial surfactants and PEO chains on a conducting material, a first electrochemically pre-functionalization step was performed (it ends with a highly reactive –Ar-SO_2Cl coating). Aryldiazonium salts were formed in-situ from a starting amine, the sulfanilic acid (5 mM), in the presence of one equivalent of $NaNO_2$ in HCl (1 M) aqueous solution. The aryldiazonium salt reduction was carried out using cyclic voltammetry (CV). After this electrochemical step, the surface was rinsed in ultrapure water for 5 min. The electrode (-Ar-SO_3H) was then functionalized (-Ar-SO_2Cl) by immersion in a PCl_5/CH_2Cl_2 solution (5 mM) for 5 minutes. This -SO_2Cl group is known to strongly react with weak nucleophilic nitrogen or oxygen groups, to form respectively sulphonamides or sulfonic ester linkers. Surfaces were then further rinsed in pure acetone for 5 min. The scheme of the reactions is shown in Figure 1 a.

Pre-functionalization assisted by CV.

The irreversible reduction of aryldiazonium salts in aryl radical ($N_2^+ \rightarrow Ar^{\bullet}$) and the electro-grafting of this radical are completed by CV on a potential range going from 0.2 V to -0.2 V/ Ag|AgCl swept at a scan rate of 50 $mV.s^{-1}$ (Figure 2 a shows the corresponding voltammograms on gold). This was done in a sulfanilic acid 5 mM, one equivalent of $NaNO_2$ in HCl 1 M aqueous solution. The reduction of aryldiazonium salts to free radicals produces a reduction band in the potential window: 0 to 0.1 V. As previously demonstrated [25], a quasi-

monolayer of para-benzenesulphonyl acid (-Ar-SO_3H) forms after reaction between the amine and $NaNO_2$. This was also confirmed in the following x-ray reflectivity experiments. On gold, a molar surface coverage of $\Gamma \sim$ 3-4 x10^{-10} mol.cm^{-2} was reported[13] and higher densities were reached up to an ideal close-packed monolayer (12 x10^{-10} mol.cm^{-2} on carbon electrodes[37]).

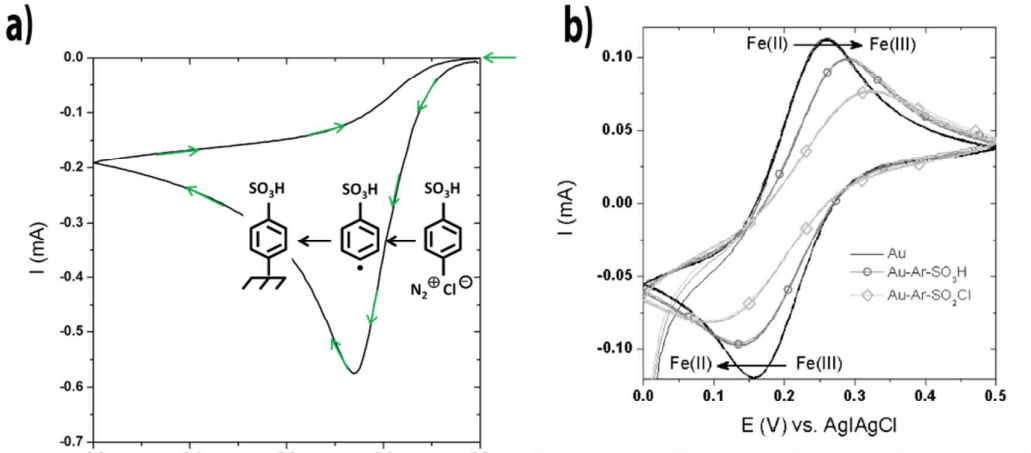

c)

Surfaces	E_{red} ($V_{Ag\|AgCl}$)	E_{ox} ($V_{Ag\|AgCl}$)	ΔE ($V_{Ag\|AgCl}$)
Au	0.16	0.26	0.1
Au-ArSO_3H	0.14	0.29	0.15
Au-ArSO_2Cl	0.09	0.32	0.23

Figure 2. a) Cyclic voltammetric curve of the formation of aryldiazonium free radicals and electrografting to the gold surface (black line); b) CV curves (100 mV/s, 10cycles) of Au, Au-ArSO_3H and Au-ArSO_2Cl surfaces, measured with 5mM $[Fe(Cn)_6]^{3-/4-}$ in a KCl 0.1M solution; c) Reduction and oxidation peaks measured.

Functionalization with –OH terminated surfactants. The grafting of surfactants was obtained by dipping the gold or chromium activated electrodes (Ar-SO_2Cl surface state) in an acetonitrile solution of solubilised surfactants at 8 10^{-5} M (*i.e.* ~1% w/w fraction). Long dips of 17 to 25 hours were carried out in Brij58, PEO or mixtures of both (then keeping the total molar concentration fixed but varying molar ratios: Birj/PEO: 25 %, 50 % and 75 %). We refer to such samples with these Brij58/PEO ratios. Other electrodes were prepared by a first dip in a 100% Brij58 solution for 17-25 hours and a second dip in a 100 % PEO solution for a day, with a rinsing in acetone and drying between 1st and 2nd steps. Brij functionalizations were also tested in water and the mass intake was monitored using a pre-functionalized gold QCM sensor (Figure S-3). The data shows that Brij-58 molecules self-assemble at the interface and form bilayers in water with an area per molecule of ~ 80 Å², close to the value obtained for Brij-58 micelles above the CMC (critical micelle concentration, see supporting information *Grafting kinetics of Brij surfactants in water monitored by QCM,* Figure S-4). All electrodes were then finally rinsed and sonicated in acetone and water for 5 min to remove unbound molecules.

Contact angle (CA) measurements. Water contact angles were measured using a homemade set-up with a halogen source and a telecentric lens on the source and camera pathways. Raw and functionalized chromium thin films deposited on glass were first washed

with dichloromethane, acetone and dried under strong filtered air flow. Contact angles were measured with a precision of 0.1°. At least 5 drops of 1 µL were deposited on separated regions over the surface to obtain an average value for each sample. Ultra-flat thin metal films were used for CA measurements because of their large enough area (2.25 cm²), this excludes small hand polished standard gold electrodes.

AFM. Atomic force microscopy images were measured on a Dimension Nanoscope V from Veeco™ (Bruker) operating in tapping mode at room temperature with silicon AFM probes (Nanosensor PPP-NCHR-W tip). The instrument runs with the Nanoscope 7.20 software and all images were processed using the Gwyddion freeware (version 2.27). For each sample, several zones were systematically imaged over scanned areas of 1×1 µm², 5×5 µm² and 10×10 µm², in order to estimate the surface homogeneity and topography at different length scales.

X-ray specular reflectivity. X-ray reflectivity (XRR) measurements were conducted using a PANalytical Empyrean X-Ray diffractometer running at 40 kV and 30 mA (Cu-Ka radiation reflected on a parallel beam x-ray monochromator at 0.154 nm). Reflectivity scans, data treatment and fitting analysis are presented in the supporting information, *X-ray reflectivity measurements of the bare chromium thin films.*

Electrochemical impedance spectroscopy (EIS). All electrochemical experiments were performed on a potentiostat/galvanostat model VMP2/Z system (Bio-Logic™) monitored by ECLab software and using a Ag|AgCl reference electrode. EIS experiments were carried out at room temperature with a three electrodes teflon flow cell connected to a potentiostat/galvanostat model VMP2/Z system (Bio-Logic™). Non-faradaic measurements were carried out in NaCl 0.15 M. A 25 mV amplitude sine wave was applied to the working electrode at 0 V bias versus the reference electrode (RE, a saturated silver-silver chloride [Ag|AgCl|NaCl(aq,sat)] electrode from Bio-Logic™, model RE-3V) that was screwed in between the auxiliary electrode (AE, gold coated quartz from Bio-Logic QCM sensors) and the working electrodes (WE, a chromium-coated glass substrate). The AE was set at 5 mm from the WE and could be used for simultaneous QCM mass measurements. The frequency range analysed goes from 0.1 Hz to 200 kHz and was always scanned from high to low frequencies. Data were fitted using a homemade program using the Matlab software and theoretical models described below. Data are often presented in the Nyquist plot (Im(C) vs Re(C), where $C=C(\omega)$ is the frequency-dependent capacitance of the electrode where ω is the angular frequency, $\omega=2\pi f$, with f the frequency in Hertz).

EIS measurements in the faradaic mode were also carried out on the elaborated electrodes, using a solution containing equal concentrations of oxidized and reduced forms of the $Fe(CN)_6^{3-/4-}$ redox couple (ferricyanide/ferrocyanide ions), in a supporting electrolyte of 0.1 M KCl. For the EIS measurements, a 25 mV amplitude sine wave was applied to the electrode at the formal potential of the redox couple, where the anodic and cathodic currents are equivalent ($E_{1/2} = (E_{p,a}+E_{p,c})/2$, with $E_{p,a}$ and $E_{p,c}$ being respectively the anodic and cathodic peak potentials for the reversible electrochemical signal of the given redox couple.

EIS data fitting: Models and equivalent circuits. In order to simplify the calculations of impedances, the results obtained from the periodic perturbation of an electrical circuit were represented using complex notation. The EI spectra were modeled using different equivalent circuits for the functionalized working electrode surfaces, shown in the inset of the corresponding figures in non faradaic or faradaic modes.

EIS in non faradaic mode. The impedance of this circuit, consisting of a series connection of the resistance R_s with the parallel connection of R_{ci} and $CPE_{dc,}$ is given as [38] :

$$Z_{Tot} = R_S + \frac{1}{(j\omega)^{\alpha_1} Q_1 + \frac{1}{R_2}} \quad in\ \Omega \cdot cm^2 \tag{1}$$

The contribution of each term is shown in Figure S-6 in the supplementary information.

Modeling EIS in faradaic mode. In presence of a redox couple used to probe the interface, the formation of the ionic Helmotz double layer (here represented by a pseudo-capacity constant phase element, CPE_{dc}) and the resistive charge transfer of the probe (R_{ct}), come at comparable timescales. The measured charge transfer depends on the diffusion of the probe to the electrode ($Z_{faradaic} = CPE_W + R_{ct}$) is modelised using a so-called "Randles" circuit (inset Figure 3 a). The circuit consists then of a series connection of the resistance R_s with the parallel connection of CPE_{dc} and $CPE_W + R_{ct}$. Its total impedance is given as :

$$Z_{Randles}(\omega) = Z_S + \frac{1}{\frac{1}{CPE_{dc}} + \frac{1}{Z_W + Z_{Rct}}} \quad in\ \Omega \cdot cm^2, \tag{2}$$

with CPE_{dc} being the double layer impedance: $CPE_{dc} = (j\boldsymbol{\omega})^{\boldsymbol{\alpha_1}} Q_1$ and Z_{Rct} being the charge transfer impedance of the redox probe at the intzrface: $Z_{Rct}(\omega) = R_{Ct} = RT/nFi_0$ where i_0 corresponds to the electrode charge current (i_0). At low frequencies, a so called "Warburg impedance" ($Z_W = Z_{W,Ox} + Z_{W,Red}$) is measured for the diffusion and corresponds to a CPE with $\alpha = 0{,}5$ and Q=W. Supposing that the two redox species have a semi-infinite diffusion and a concentration near the interface following Nernst equation: $C_{Ox}(0)/C_{Red}(0) = \exp(nF(E - E^0)$, the Warburg impedance states [39]:

$$Z_W(\omega) = \frac{1}{\sqrt{j\omega}\, W} = \frac{\sigma\sqrt{2}}{\sqrt{j\omega}} = \frac{\sigma}{\sqrt{\omega}}(1 - j)\ in\ \Omega \cdot cm^2 \tag{3}$$

$$\text{where } \frac{1}{\sqrt{j}} = \frac{1}{\sqrt{2}}(1 - j) \text{ and } \frac{1}{W} = \sigma\sqrt{2},$$

with the mass transfer coefficient σ being:

$$\sigma = \sigma_{Ox} + \sigma_{Red} = \frac{RT}{\sqrt{2}\, n^2 F^2 S}\left[\frac{1}{\sqrt{D_{Ox}} C_{Ox}(0)} + \frac{1}{\sqrt{D_{Red}} C_{Red}(0)}\right] \ in\ \ \Omega s^{-1/2}\, cm^2 \tag{4}$$

with R the molar gaz constant (8.314 J mol^{-1} K^{-1}), T the temperature (295 K), n the number of electrons of the reaction, F the Faraday constant (96485.333 C mol^{-1}), S the electrode surface (cm^2), $C_{Ox}(0)$ and $C_{Red}(0)$ are the initial concentrations of the redox couple (mol/cm^3), and D_{Ox} and D_{Red} their diffusion coefficients respectively (cm^2 s^{-1}).

Supposing concentrations and diffusion coefficients near the electrode are close to those in the bulk [40], the global diffusion coefficient is given as:

$$D = \left(\frac{\sqrt{2}RT}{n^2F^2S}\,\frac{1}{C\,\sigma}\right)^2 \quad \text{with} \quad \sigma = \sigma_{Ox} + \sigma_{Red}\ .\ (\mathrm{m^2\ cm^{-1}}) \tag{5}$$

Fit of the EIS data. The EIS data were recorded in the form of the amplitude and phase of impedance as a function of the frequency, *f*. They were fitted in the form of complex numbers in the C_Nyquist representation: Re(C) and Im(C) versus *f* with a homemade Matlab routine based on the model circuits. Fits of the same data in two other representations: Z_Nyquist representation, Re(Z) and Im(Z) versus *f* and Bode representation, |Z| and phase(Z) versus *f,* are compared in Figure S-5 of the supporting information, *Fit of the EIS data in different representations*. The best fits of the same data, obtained for each of the three representations are compared in confidence limits of the best-fit model parameters were quantified by evaluating the variance-covariance matrices of the Levenberg-Marquardt algorithm employed in a nonlinear χ^2 minimization between model and data.

Results and Discussion.

In order to determine the optimal reaction conditions for the chemistry envisioned, we first used a model interface. In this case, we functionalized standard gold electrodes. The same chemistry worked as well on ultra-flat and thin chrome films. As discussed in following sections, those exhibited a much better sensitivity of the measured parameters according to the surface states.

Interfacial charge transfer of a redox probe (CV and EIS in faradaic mode):

Pre-functionalization of gold electrodes (Au, Au-Ar-SO_3H and Au-Ar-SO_2Cl). The pre-functionalized electrodes, namely metal-$ArSO_3H$ and metal-$ArSO_2Cl$, were firstly studied using CV through the electrochemical signal of a reference[41-43] redox couple in solution [$Fe(CN)_6^{3-/4-}$]. Current resulting from the electronic transfer between the redox probe and the surface, and its kinetics, are monitored by CV on a potential range from 0.2 V to -0.2 V/Ag|AgCl at a gold electrode (vs. Ag|AgCl reference electrode) with a scan rate of 100 $mV.s^{-1}$ (Figure 2 b). The cyclic voltammograms of the electrochemical processes show a reduction peak at E_{red} = 0.16 V corresponding to the reduction of Fe(II) in Fe(III) and an oxidation peak at E_{ox} = 0.26 V corresponding to the oxidation of Fe(II) in Fe(III). The lowest is the gap from peak to peak (ΔE), the fastest is the electronic transfer. The electronic transfer slows down (Figure 2 c) and peaks intensity decreases after the pre-functionalization. This is due to the metal surface passivation, as a consequence of the aryldiazonium salts reduction (Au to Au-$ArSO_3H$) and to the conversion -SO_3H groups to -SO_2Cl after contact with PCl_5. Even if it is quite thin, the organic layer reduces the electronic transfer (increase in resistivity). The probe interactions with the surface also changed since -$ArSO_3H$ should have a global negative charge at pH~7 (pKa ~3.24 [44], whereas Au-$ArSO_2Cl$ come with a lower

global negative charge and Au-$ArSO_2Cl$ surface shows a less hydrophilic character than Au-$ArSO_3H$.

To probe the ions dynamics and the surface electrochemical properties at different steps of the functionalization, we measured the EIS data. All spectra were well fitted using a simple $R_S(CPE_{dc}(R_{Ct}\,CPE_W))$ model circuit (insert Figure 3 a), and best fit-parameters are given in Table 1. The Figure 3 a shows how the top semi-circles of the measured capacitance are related to the circuit characteristic pulsation: $\omega_{c1} = 1/(R_{CT}C_{dc})^{1/\alpha}$. At higher than ω_{c1} frequencies, the charge transfer to the electrode is controlled by the reaction kinetics and depends on the tension while at lower than ω_{c1} frequencies, the current is limited by the diffusion speed of the redox species to the electrode (in the so-called "Warburg regime" where the slope of the –Im(Z) versus Re(Z) curve is equal to one). The EIS data, plotted in the form of a impedance, exhibits here a slightly flattened semi-circular shape, consistent with the capacitive behaviour of a nearly ideal insulating dielectric layer (α = 0.89 while 1 would be expected for a purely capacitive behaviour giving a perfect semicircle). This behaviour is consistent with surface inhomogeneities, such as roughness. The cell resistance, R_S, marks the starting point of the semi-circle on the x axis, and only depends on the electrolyte and cell geometry used here. The charge transfer resistance R_{ct} is the most affected parameter by the functionalization, since it increases when it becomes more difficult for the electrochemical probe to exchange electrons with the metal interface. Once cleaned, we obtained R_{ct} < 10 Ω cm² for gold and R_{ct} scales with the inverse of the kinetics constant for the redox couple $[Fe(Cn)_6]^{3-/4-}$:

$$k_{RedOx,app} = \frac{RT}{n^2F^2S}\,\frac{1}{C_{RedOx}\,R_{ct}} \qquad (6)$$

On clean gold electrodes we obtained $k_{RedOx,app}$ = 0.0011 cm/s.

On pre-functionalized Au-Ar-SO_3H surfaces, we observed as expected that the charge transfer resistance increased (R_{ct} ~ 25 Ω cm²) due to the organic passivation of the metal interface. The last pre-functionalization step introduces an Au-Ar-SO_2Cl surface layer, increasing even more the charge transfer resistance (R_{ct} ~62 Ω cm²). This is consistent with the CV results. In addition, the probe diffusion to the surface appears to be more and more resistive (α_W < 0.5 [45]), certainly due to the more hydrophobic nature of -$ArSO_2Cl$. For insulating coatings, it is usual to assimilate a charge transfer resistance R_{ct} to the presence of patches where bare metal is still accessible to the probe (with a possible diffusion limited access). In this case, one can estimate an apparent coated surface fraction: $\phi_{AuArX} = 1 - R_{ct,Au}/R_{ct,AuArX}$ and the gold surface fraction: $\phi_{Au} = 1 - \phi_{AuArX}$. Following this, one obtains: $\phi_{AuArSO_3H} = 0.78$ and $\phi_{AuArSO_2Cl} = 0.91$ for the pre-functionalized surfaces, which reflects a homogeneous surface covering in both cases and a different ability to hinder the charge transfer of the probe for –$ArSO_3H$ and -$ArSO_2Cl$, explaining that $\phi_{AuArSO_3H} < \phi_{AuArSO_2Cl}$. The EIS spectrum of the gold surface is similar to the one obtained by Janek *et al.* [42], who used a five times more diluted probe as well as another salt (0.5M $Na^+ClO_4^-$),

resulting in a mass transfer coefficient, σ, ten times higher ($\sigma_{Au,Janek}$ = 133 Ω $s^{-0,5}$ cm^2) and thus in a diffusion coefficient of the redox probe equal to D_{Ox}=7.63 10^{-6} cm^2s^{-1} and D_{Red}=6.32 10^{-6} cm^2s^{-1} [42,46]. In our case, the estimated diffusion coefficients of the probe $[Fe(CN)_6]^{3-/4-}$ are higher and not drastically affected by the surface state, as expected for such ultra-thin coatings. We also expect that the concentration and the diffusion coefficients of the probe are the same near the electrode and in the bulk solution [40].

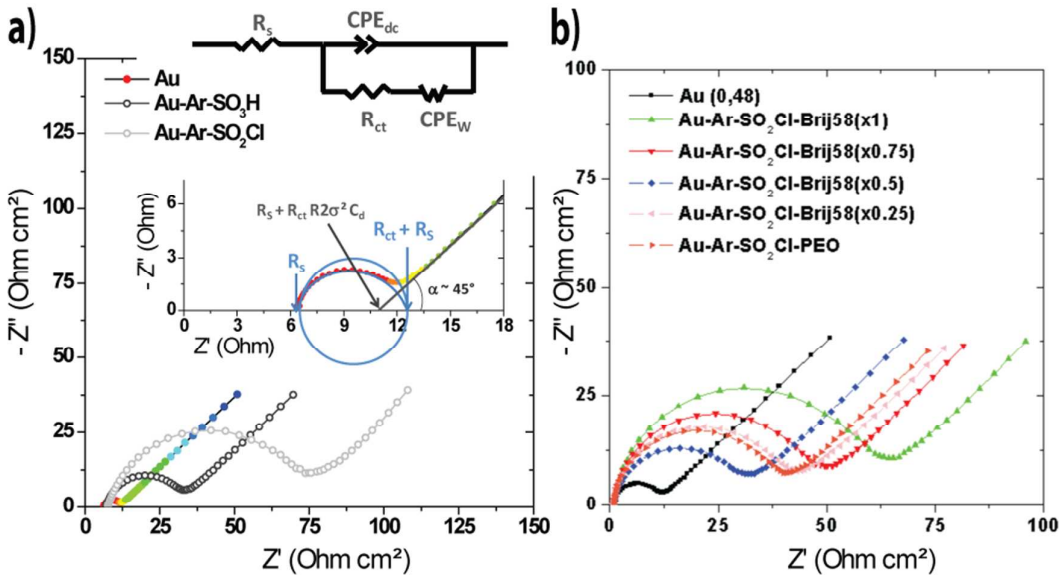

Figure 3. a) Z_Nyquist representation of the EIS data measured in faradaic mode for cleaned gold and pre-functionalized electrodes (Au-ArSO_3H and Au-ArSO2Cl) with a 5mM $[Fe(Cn)_6]^{3-/4-}$ and 0.1 M KCl solution; Inset: Equivalent circuits used for the modelling of the electrochemical impedance spectra in the faradaic mode; b) Z_Nyquist representation of the EIS data of functionalized electrodes Au-ArSO_2-58 (xi) –PEO9-CH3 (1-xi) with i = 1 ; 0,75 ; 0,5 ; 0,25 ; 0 in 5mM $[Fe(Cn)_6]^{3-/4-}$ in 0.1 M KCl. Surfactant concentration used for functionalization: C = 0,09 mmol/L .

Surface states :	Au	Au-Ar-SO_3H	Au-Ar-SO_2Cl	Au-Ar-SO2-Brij58…				
				100%	75%	50%	25%	0%
Q (µF $s^{\alpha-1}$ cm^{-2})	235	420	405	304	301	238	540	357
α_{dc}	0.89	0,88	0,85	0.86	0.86	0.85	0.80	0,83
σ (Ω $s^{-0,5}$ cm^2)	12	12	13	16	17	16	14	17
D_{RedOx} (10^{-6} cm^2s^{-1})	*37*	*38*	*29*	*21*	*18*	*20*	*25*	*17*
α_W	0.50	0.50	0.43	0.5	0.49	0.5	0.48	0.46

R_{ct} (Ω cm²)	5	24	62	58	45	28	39	36
$k_{RedOx,app}$ (cms^{-1})	*0.01*	*0.002*	*$8.5.10^{-4}$*	*0.0009*	*0.0012*	*0.0018*	*0.0013*	*0.0014*
ϕ_{AuArX} (%)	*100*	*78*	*91*	-	-	-	-	-
f_{c1} (Hz)	*291*	*29*	*12*	*17*	*23*	*56*	*19*	*29*
f_D (Hz)	*2*	*2*	*0.02*	*0.03*	*0.05*	*0.1*	*0.05*	*0.07*

Table 1. Best-fit parameters obtained for the EIS data measured in the faradaic mode on gold, pre-functionalized electrodes (Au-Ar-SO_3H Au-Ar-SO_2Cl) and functionalized (Au-ArSO_2-58 (xi) –PEO_9-CH_3 (1-xi) with i = 1 ; 0,75 ; 0,5 ; 0,25 ; 0 in 5mM $[Fe(Cn)_6]^{3-/4-}$ in 0.1 M KCl. Surfactant concentration used for functionalization: C = 0,09 mmol/L). Fitted parameters are: Q: pseudo-capacity, R_{ct} and R_s : charge transfer resistance and cell resistance (~7 Ω cm², not given), σ: mass transfer coefficient. Calculated associated characteristic frequencies of the circuit are also given: f_{c1} at low frequencies and f_D at high frequencies, and the electrode surface coverage for pre-functionalizations.

Surfactant functionalization of gold electrodes (-SO_2-Brij or PEO or mixtures). The activated pre-functionalized Au-Ar-SO_2Cl electrodes were then functionalized with Brij58 and/or PEO at different molar ratios, and studied in the same way using EIS in faradaic mode (EIS data are shown in Figure 3 b with best fit- parameters reported in Table 1). For all surface compositions (x=0 to 1), the fit parameter α, that measures the electrochemical surface homogeneity, is close to 0.86 not far from the one obtained for bare cleaned gold. The values of α_W also remain close to 0.5, indicating a linear diffusion of the redox species with the electric field near the interface with values between 18 and 25.10^{-6} cm² s^{-1} calculated from the Warburg impedance for the redox couple in agreement with the literature [42,46]. On the contrary, noticeable changes of R_{ct} are evidenced with the nature of the graft molecule: the charge transfer resistance increases with increasing fraction of Brij58, so correspondingly the electrochemical charge transfer constant ($k_{RedOx,app}$) drops.

The CV and EIS methods can be thus considered as a very effective way to monitor the surface modification at each step. For this we used the $Fe(CN)_6^{3-/4-}$ couple, an inner-sphere redox probe that needs to be in close contact with the surface to allow electron transfer.

Charge transfer resistance and contact angles. Since the faradaic charge transfer resistance R_{ct} varies with the nature of the molecule grafted on the electrode, we wondered how it correlates with the interface water affinity. For this purpose ultra-flat electrodes obtained from the thin chromium films were used (with a roughness below a nm) to measure contact angle with pure water for the different surface states (bare cleaned electrode, Ar-SO_3H, Ar-SO_2Cl, pure Ar-SO_2-Brij58, pure Ar-SO_2–PEO_9-CH_3 and their mixtures x=0.75, 0.5 and 0.25). The static water contact angles are plotted on the same graph than the R_{ct} values (Figure 4 a) showing a good correlation of these two physical quantities. The comparison shows a slight trend: the charge transfer resistance is smaller for the more hydrophilic functionalizations, but the values remain higher than on the bare electrode.

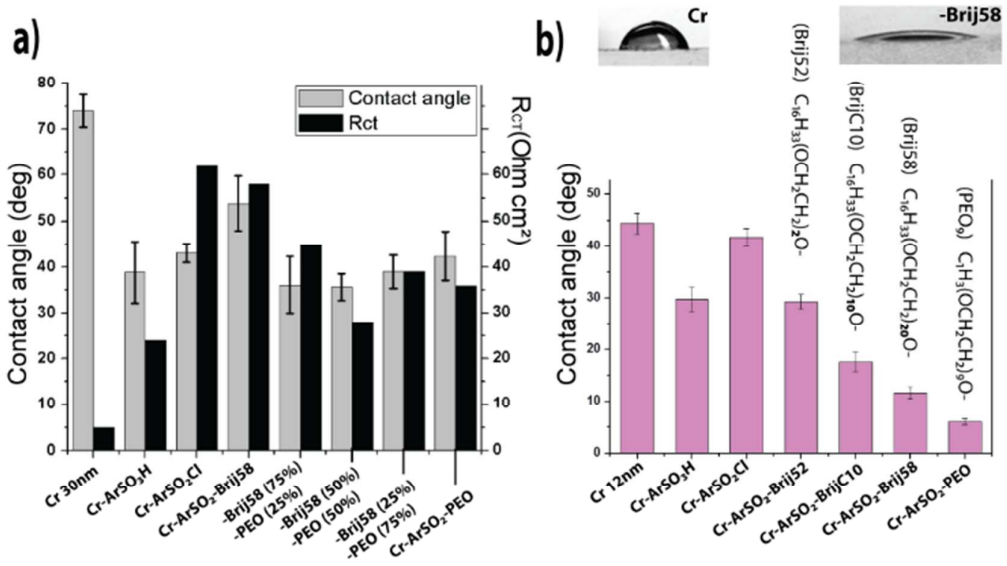

Figure 4. a) Comparison between faradaic charge transfer resistance (R_{ct}) and wettability of different electrode surface states (*cleaned chromium thin film of 30nm, -Ar-SO_3H, -Ar-SO_2Cl, -Ar-SO_2-Brij58, -Ar-SO_2–PEO_9-CH_3 and their mixtures*); *b) Contact angle measurements of water droplets of 1µL deposited on bare and functionalized chromium. The error bare comes from measurements of many droplets per sample and several samples for each surface state. Representative pictures are also shown.*

Ions dynamics at the interface (EIS in non-faradaic mode).

Pre-functionalization of electrodes (-SO_3H and -SO_2Cl on Au or Cr). The non-faradaic EIS mode is an attractive method for biosensors since no redox species are needed and the capacitance signal of the electrode/electrolyte interface changes with modifications of the ionic double layer and ions dynamics under E-field. We studied the gold and chromium plate electrodes at the different steps of the functionalization using EIS with a NaCl 0.15M solution. The data for the pre-functionalization steps are shown in Figure 5 a (Au, Au-$ArSO_3H$, Au-$ArSO_2Cl$) and can be well fitted using the equivalent circuit shown and that is widely used for modelling dielectric properties of single component alkanethiol SAMs [3] and insulating solid-supported phospholipid bilayers [38]. This circuit comes with a low frequency purely resistive regime below $f_{c1} = 1/(R_{ci}Q_{dc})^{1/\alpha}2\pi$ where $|Z_{Tot}| \rightarrow |R_{ci} + R_S|$. This cut-off frequency appears in our case at lower frequencies than our first measured points (starting at 0.1Hz), which means that the interfacial capacity did not totally charge during the potential cycles. At frequencies higher than $f_{c2} = 1/(R_{ci}R_SQ/(R_{ci} + R_S))^{1/\alpha}2\pi$, a second transition is expected towards a purely resistive regime limited by the global cell resistance ($|Z_{Tot}| \rightarrow |R_S|$). This is clearly identified in the data plotted in the Z_Bode representation (f_{c2} between 495 and 1307 Hz for the different samples). The gold electrode EIS signal exhibits a semicircular shape, expected for a capacitive behaviour of a near-ideally insulating dielectric layer. The mid frequency minimum of the circle does not completely return to the x axis like it would with a pure capacitive circuit. A low-frequency tail follows from the presence of a parallel resistive branch (R_{ci}) in the circuit. The charges going through R_{ci} shunt the capacity

branch like a current leakage. In that sense it is often assimilated to the presence of defects in the plates of the interfacial capacitor. The fit parameters of the model are: a constant phase element coefficient, CPE (corresponding to an impedance $Z_{CPE}=1/CPE(i\omega)^{\alpha}$) in F cm^{-2} $s^{\alpha-1}$; the exponent α and the two resistances R_{ci} and R_S (Figure 5 a). Fitting the data with a simple $R_s(R_{ci}CPE)$ equivalent circuit on our extended frequency range (0.1Hz to 2.10^5Hz) makes it difficult to perfectly reproduce the low frequency tail. However, if lowest frequencies are excluded (rarely measured in the literature with EIS starting generally at 1Hz and ending at 6.5 10^4Hz, [38]), the model perfectly fits the data. In another try, we fitted the data with addition of a CPE element in the parallel resistive branch ($R_s(CPE(R_dCPE_d))$). This model was used by McGillivray, Valincius and co-workers [38,47] to model tBLMs (tethered bilayers lipid membranes) where R_d and CPE_d are generated by defects in the organic layer. This model did not improve the fits so that the simplest circuit was used (best fit-parameters given in Table 2). With the pre-functionalization modifications, a reduction of the resistance (R_{ci}) occurs and should be interpreted as the increase of the fraction of charges that shunt the capacity branch and do not accumulate to the capacitor plates. An increase of the semicircular diameter was also identified, compared to bare gold, and the mid-frequency dip of the spectra in the C_Nyquist representation continued to lift off the x axis with a longer low-frequency tail. The bare gold surface presents the weakest double layer capacity (19 µF cm^{-2}). Note that a large dispersion of values is found in the literature for plane metal electrodes, in between 10 and 60 µF cm^{-2} (McGillivray et al. reported for C_{Au}~10µF cm^{-2} and C_{Pt} = 40 µF cm^{-2} for platinum [38]). The organic layer enhances the interfacial capacity and the Au-Ar-SO_3H surface gives the higher value (C ~ 40,7 µF cm^{-2}), like in faradaic mode. This denotes a better ability to accumulate charges on the armatures certainly due to the more hydrophilic character of the interface and a possible negative charge at pH~7 (pKa ~3.24 [44]). This increase was expected from the organic additional contributions to the capacitance (Q_{dc} on gold becomes $Q_{Au\text{-}ArX} = 1/(Q_{Ar}^{-1}+Q_{SO3H}^{-1}+Q_{dc}^{-1}$ with pre-functionalization) [48] if one considers that the ionic double layer is the same on top of both surfaces). The change from Ar-SO_3H to the less hydrophilic Ar-SO_2Cl group follows this trend and gives an intermediate behaviour with gold corresponding to the smaller capacity, higher R_{ci} and higher hydrophobicity.

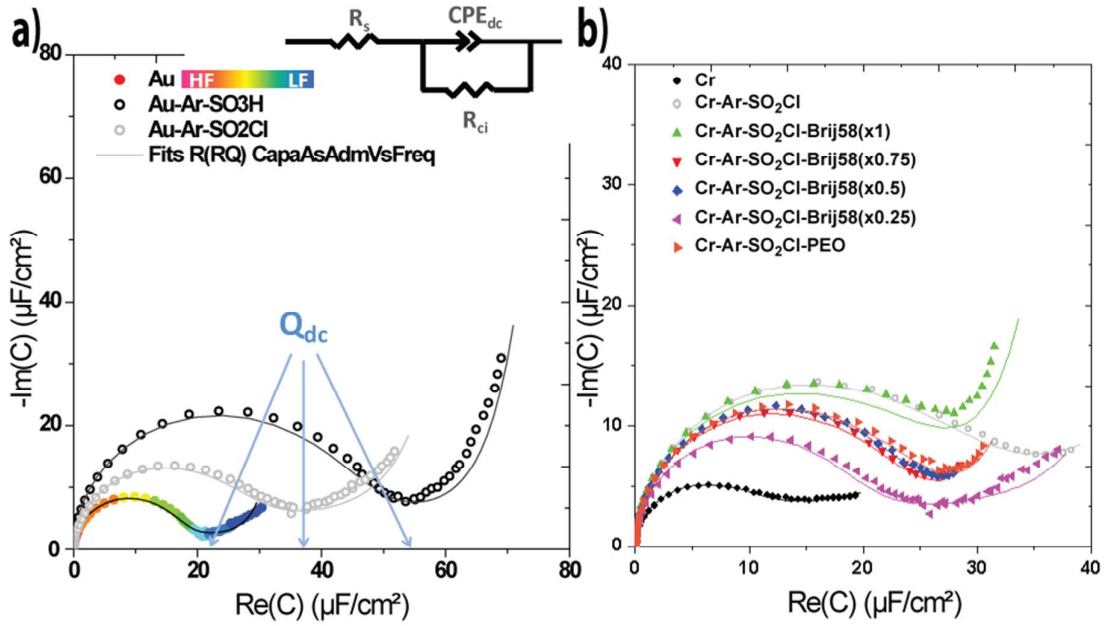

Figure 5. a) Complex plane plots of total capacitance of gold and pre-functionalized electrodes Au-ArSO$_3$H and Au-ArSO2Cl in 150 mM NaCl; Inset: Equivalent circuits used for the modelling of the electrochemical impedance spectra in the non-faradaic mode; b) Complex plane plots of total capacitance of chromium and functionalized electrodes: Cr-ArSO$_2$Cl, Cr-ArSO$_2$-Brij58(xi) with i the ratio of Brij58 and 1-i the ratio of PEO$_9$-CH$_3$. Solid lines correspond to the best fits to the data.

Fit parameters. *Deduces parameters are in italic* ($R_S(R_{Ci}CPE_{dc})$)	Au	Au-Ar-SO3H	Au-Ar-SO2Cl	**Cr**	Cr-Ar-SO$_3$H	Cr-Ar-SO$_2$Cl	Cr-Ar-SO$_2$-Brij58	Cr-Ar-SO$_2$-Brij58 (75%)	Cr-Ar-SO$_2$-Brij58 (50%)	Cr-Ar-SO$_2$-Brij58 (25%)	Cr-Ar-SO$_2$-PEO$_9$
Q (µF s$^{\alpha-1}$ cm^{-2})	44	69	52	19	35	38	33	29	28	27	31
C (µF cm^{-2})	*19*	*40*	*24*	*9*	*25*	*26*	*24*	*22*	*22*	*13*	*22*
α	0.91	0.93	0.91	0.87	0.91	0.90	0.91	0.93	0.93	0.92	0.92
R_{ci} (kΩ cm²)	204	55	151	10 956	1 500	986	120	488	698	540	362
R_S (Ω cm²)	6.2	7.9	8.3	548	673	776	1234	963	1788	850	773
f_{c1} (Hz)	*0.014*	*0.038*	*0.016*	*3.10^{-3}*	*2.10^{-3}*	*3.10^{-3}*	*0.034*	*9.10^{-3}*	*2.10^{-3}*	*9.10^{-3}*	*10^{-2}*
f_{c2} (Hz)	*1307*	*495*	*800*	*30.8*	*9.5*	*7.9*	*5.3*	*7.7*	*4*	*9.8*	*9.3*

Table 2. Best-fit parameters of the EIS data (cleaned bare gold and chromium, pre-functionalized electrodes : -Ar-SO$_3$H and -Ar-SO$_2$Cl; and functionalized electrodes Cr-Ar-SO$_2$Cl, Cr-ArSO$_2$-Brij58(xi) with i the ratio of Brij58 and 1-i the ratio of PEO$_9$-CH$_3$): Q : pseudo-capacity, C_{dl} : double layer capacity, R_{ct} and R_s : resistance to ionic diffusion and cell resistance, σ : mass transfer coefficient, f_{c1}: low characteristic frequency, f_{c2} : high characteristic frequency).

Similar pre-functionalizations were realized on chromium thin films and studied in the same way with EIS in the non-faradaic mode. The cell resistance (R_s) increased by two orders of magnitude in comparison to the standard gold electrodes. This phenomenon restricted the access to high frequency domain ($f < f_{c2} = 1/(R_{ci}R_S Q/(R_{ci} + R_S))^{1/\alpha}2\pi$, above the impedance follows R_s). The EIS data of the chromium and Cr-ArSO_2Cl surfaces are plotted in Figure 5 b in the C_Nyquist representation (black and grey curves, respectively). The raw electrode signal could be well fitted with a simple $R_s\,CPE_{dc}$ model circuit. Using a $R_s(R_{ci}\,CPE_{dc})$ model ended with a high R_{ci} value so that the $1/R_{ci}$ term was negligible for the experimental frequency range (Table 2). Indeed, the behaviour of a $R_s(R_{ci}\,CPE_{dc})$ circuit is expected at frequencies smaller than $f_{c1} = 1/(R_{ci}Q_{dc})^{1/\alpha}2\pi \sim 3\ 10^{-3}$Hz in our case. Thus, the measured signal comes mostly from the double layer capacity ($C_{Cr,dc} \sim 9$ µF cm^{-2}) and its dispersion along the surface which is not negligible ($\alpha = 0.86$). Given the good planarity and roughness of the chromium electrodes, this distribution of the surface capacity should be related to the presence of chromium oxide Cr_2O_3 heterogeneities at the interface. Note that even with oxidized interfaces, the electro-grafting worked and the organic coating leveled out some of the difference between Cr_2O_3 and metal Cr. The double layer capacity on chromium films is half of the one measured on gold but it increases with pre-functionalizations Cr-Ar-SO_2Cl or Cr-Ar-SO_3H to similar values than the ones measured on gold modifications ($C \sim 25$ µF cm^{-2}). The α exponent increases as well indicating a better surface homogeneity and this is somehow expected since the electro-grafting is effective both on chromium and chromium oxides [49]. The most noticeable result from the EIS data analysis of chromium ultra-flat electrodes is that R_{ci} is much higher than on standard gold. Thus, the EIS signal is capacitive with no parallel leakage current, so that most of the ions are contributing to the interface capacity frames.

Functionalized electrodes (grafting surfactants: -SO_2-Brij; or –PEO; or mixtures). The dynamics of ions near the electrode are affected by the functionalization with surfactants or small PEO chains. The pre-functionalized gold and chromium electrodes were functionalized with the same solutions of pure Brij58, pure PEO and mixtures. We noticed that the EIS data and resulting fit-parameters are much more dependent to the molecule grafted on the flat chromium electrodes than onto the rough gold standard electrodes. This is clearly observed for instance when comparing the parallel resistance values when varying the ratio of Birj58 and PEO_9: on gold : $R_{ci\_Brij\ x1}$ = 86 kΩ cm² ; $R_{ci\_Brij\ x0.75}$ = 77 kΩ cm² ; $R_{ci\_Brij\ x0.5}$ = 71.2 kΩ cm² ; R_{ci_PEO} = 85 kΩ cm²; and on chromium films: $R_{ci\_Brij\ x1}$ = 120 kΩ cm² ; $R_{ci\_Brij\ x0.75}$ = 488 kΩ cm² ; $R_{ci\_Brij\ x0.5}$ = 698 kΩ cm² ; R_{ci_PEO} = 362 kΩ cm². The data obtained on flat chromium electrodes (EIS curves plotted on Figure 5 b and resulting best fit parameters given on Table 2) shows now a lift-off the x axis at low-frequencies (on the right of C_Nyquist representations) due to the smaller values of R_{ci} obtained after functionalization (Table 2, Figure 5 b). All grafted molecules induced an ionic diffusion limited regime at low frequencies, as well as a smaller dispersion of capacities ($\alpha > 0.91$ which denotes a good surface homogeneity) for capacities ranging between 21.5 and 24.4 µF cm^{-2} (similar to the values measured with gold electrodes). On the contrary, the resistance R_{ci} is much higher for

the PEO_9-CH_3 coating (0.362 MΩ cm²) than for the pure Brij58 coating (0.120 MΩ cm²), both far above the value obtained for functionalized gold electrodes (~0.08 MΩ cm²). The small hydrophilic PEO coatings are thus giving a more capacitive system than the pure Brij58, that shown the lowest ability to efficiently accumulate charges and a higher fraction of ions that can diffuse in a resistive way to the electrode. This forms a parallel leakage current to the capacity that is responsible for the lifting off from the x axis of the EIS data at low frequencies (shown in Figure 5 b, green curve at low frequencies). The PEO_9-CH_3 coating is certainly more compact, homogeneous and thin. It forms a hydration layer, corresponding to the dielectric capacity of our model circuit and to a gap which is hard to cross for the ionic species of the double layer that accumulate at the interface under E-field. In comparison, the coverage of pure Brji58 is sparser and offers a thicker layer ($d_{Brij58} > d_{PEO}$ in Figure 6 c) with possible diffusion zones for the double layer ions, due to its hydrophobic alkyl chains and molecule length. Several studies of the literature reported similar behaviours for self assembled monolayers (SAMs) of synthesized lipid-PEO amphiphilic molecules. This has been exemplified by Lösche et al. who studied mixed SAMs obtained from the mixture of βME (β-mercaptoethanol) and PEO_6-$(C_{14})_2$ alkyl chains (WC14 molecules grafted on gold via thiol groups, Figure 6 b) [38]. The EIS data collected on those coatings were all quite similar at high fractions of WC14 ($1>x_{WC14}>0.7$) and well analysed with the equivalent circuit $Rs(R_{ci}\,CPE_{dc})$. Below $x_{WC14}=0.7$, a sharp increase of the diameter of the Cole-Cole semicircle was observed (Q increased from 0.9 to 9 μF cm^{-2} s$^{(\alpha-1)}$) and the resistivity dropped also drastically (R_{ci} in our model) from 20 to 0.5 MΩ cm² (Figure 6 a). This corresponds to the transition from a dense and thick monolayer to a sparse functionalization. The dense (resp. sparse) coating gives a low (resp. high) capacity ($C=\varepsilon/d$ with a high relative permittivity for alkyl chains, ε, and a high thickness, d) and a high (resp. low) resistivity to parallel ionic current leakages. In our case and even at high fractions of Brij58, our interfacial capacity values are 2 to 20 fold higher (Q~25μF cm^{-2} s$^{(\alpha-1)}$) with a lower resistance R_{ci} (of few hundreds of kΩ cm²). This is mainly due to the fact that the Brij58 molecules do not tend to form a dense monolayer in contrast to WC14 and also to the fact that Brijs have a higher relative permittivity since they are single alkyl chain molecules. The sparse Brijs plus PEO coatings formed much more hydrophilic coatings ($10°<\vartheta<30°$) than the lipid-PEO SAMs (ϑ~80° [38]). Figure 6 summarizes the different surface states and capacity values discussed above. We also attempted to scheme the link between capacity values and grafting densities. The curling of the Brij alkyl chains to the surface induces spare coatings while mixtures induce more hydrated, dense and thicker layers. This is consistent with the EIS analysis showing a net increase of R_{ci} (particularly for x_{Brij58} between 0.25 and 0.5) and a simple capacitive model circuit behavior ($R_S\,CPE_{dl}$).

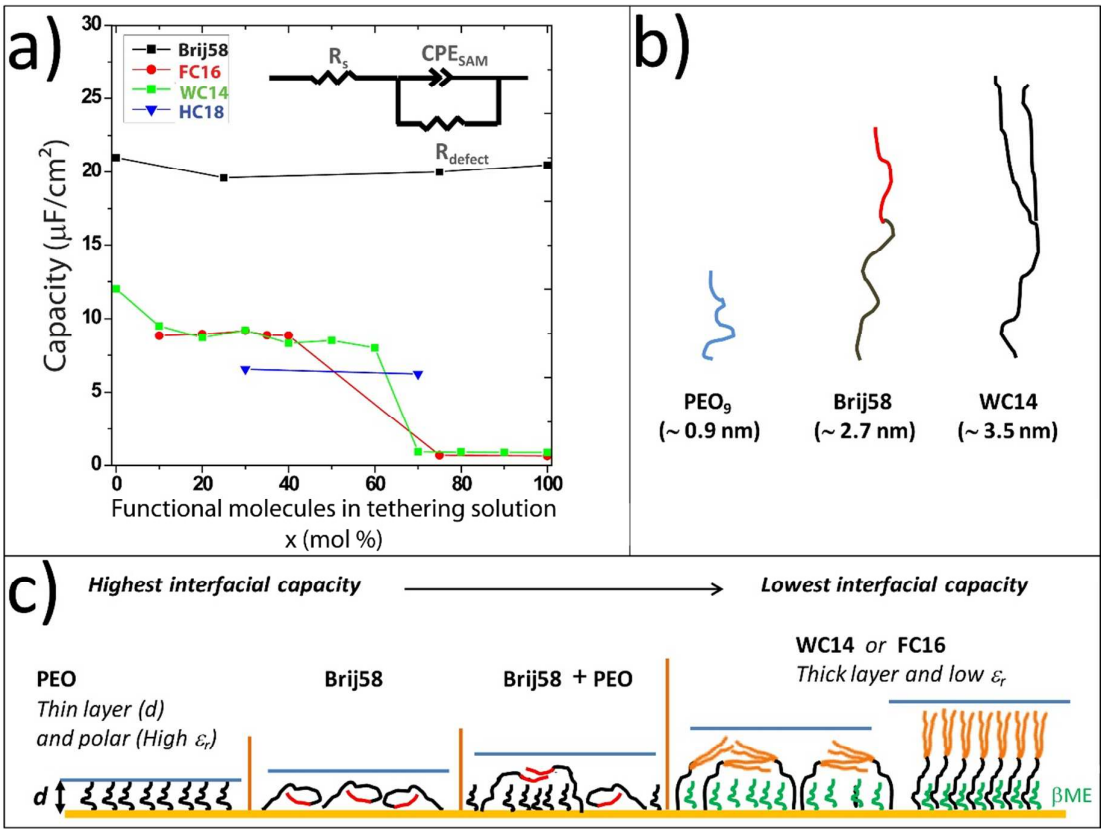

Figure 6. a) Superimposition of capacity values from Brij58:PEO functionalizations and FC16, WC14, HC18:βME SAMs as a function of the organic layer composition (proportion of tether molecules in the adsorption solution X_{tether})[38,50-51]*; b) illustration of the molecules' size (PEO_9 Brij58 according to the theory of polymers brushes, WC14 according to Heinrich et al.) ; c) Illustration of the link between capacity values and density of the layers ($C=\varepsilon_r/d$, where d is the layer thickness).*

Wetting properties of modified electrodes. The parameters extracted from the EIS analysis (faradaic and non faradaic) are directly linked to the molecular structure of the coating (density, thickness, dielectric permittivity,...) and its ability to organise ions in a capacitive double layer or to let them diffuse through in a resistive manner. In this respect, the hydrophilicity of the coating is of paramount importance since it affects the ions motions under E-field toward the metal interface. Contact angle measurement of water droplets (θ_c) is a simple and complementary way to evaluate the organic coating affinity with water. However, contact angles also dependent on the thickness, porosity and surface oxidation of the metal film, which are all varying with the deposition method. In the over all, when a bare chromium thin film exhibits a high contact angle, the pre-functionalized and the functionalized coatings will follow this trend. Our protocol was tested on chromium films obtained with different thicknesses, with thinner films generally more hydrophilic (due to higher oxidation/porosity and greater influence of the substrate long range interactions). Figure 4 b shows contact angle measurements obtained on a 12nm chromium film where surface states show particularly hydrophilic values and the same trend than the one measured on thicker chromium films. The cleaned chromium film corresponds to the more hydrophobic

surface state and the pre-functionalization by reduction of the aryldiazonium salt (-$ArSO_3H$) reduces the value by at least 30°. After activation of the surface (-$ArSO_2Cl$) the contact angle increases slightly up to 40°. Pure PEO_9-CH_3 ($H(OCH_2)_9CH3$) gave the most hydrophilic coating (θ_c~6°), as expected. The same functionalization protocol was tested using several diblock oligomers with the same blocks but of different lengths, namely: Brij58 ($C_{16}H_{33}(OCH_2CH_2)_{20}OH$), Brij52 ($C_{16}H_{33}(OCH_2CH_2)_2OH$), Brij-C10 ($C_{16}H_{33}(OCH_2CH_2)_{10}OH$). The contact angle clearly decreased with increasing PEO block length (Figure 4 b) but we do not expect that all these amphiphilic molecules adopt the same configuration at the interface and form coatings of equal density. Longer grafted PEO blocks also give more amplitude to the C_{16} alkyl chains that have to deal with unfavorable water interactions. The functionalization method proved to bind different sorts of -OH terminating commercial surfactants, resulting in versatile coatings with specific surface properties (amphiphilic and electrochemical) that go beyond the simple modification of their wetting ability.

Taking advantage of flatness and transparency of thin chromium electrodes:

x-ray reflectivity and surface scattering techniques. Thanks to the choice of chromium, which is a relatively low electronic density metal (ρ^e_{Cr} ~1.99 $e^-/Å^3$), to the low deposited thicknesses (8 to 32 nm films) and to the sub-nanometer roughness, we were able to directly probe the organic functionalizations using x-ray reflectivity measurements in air. A 16.7nm thick chromium film was characterized before and after functionalization with the thinnest coating studied, namely the Cr-Ar-SO_2-PEO_9 surface. The true specular x-ray reflectivity curves already show clear differences once plotted on the same graph (Figure 7 a). Both curves could be well fitted using a slab model that describes the electron density profile in depth (Figure 7 b, description of the fitting routine can be found in the supporting information, *X-ray reflectivity measurements of the bare chromium thin films*). The fit parameters correspond to the following characteristics of each layer: its thickness (d in Å) ; its top root mean square roughness (σ in Å) ; its electronic density (ρ^e in electrons/$Å^3$ that translates in a scattering length density Re(ρb) after multiplication by the Thomson factor r_0 = $2.81794.10^{-5}$ Å) ; its linear attenuation coefficient (that translates in the imaginary part of the scattering length density Im(ρb), which was fixed here to calculated values). The best fitting parameters are reported in Table S5 of the SI. The expected values were obtained for the metal chromium density (55.4 instead of 55.9 $e^-/Å^3$), here for a 16.7nm Cr film but also for thicker films (see supporting information). The interfacial roughnesses are 0.84nm at SiO_2/Cr and 0.99nm at Cr/air, in agreement with AFM measurements. Note that the expected density for the most stable oxide (Cr_2O_3) is 1.49 $e^-/Å^3$ and one should bear in mind that the oxidation of the Cr interfaces contributes to increasing the value of the fitted interfacial roughness, in addition to the topographic roughness. After functionalization, the fitted parameters corresponding to the substrate and metal layer were unchanged, but it was mandatory for fitting the data to add two slabs on top that were attributed to the -Ar-SO_2- monolayer (~0.5nm) and to the -PEO_9-CH_3 cushion grafted on it (h_{PEO}~1.72nm). To highlight the two

slab localisation, we also plotted the absolute value of the first derivative of the electron density profile in depth (Figure 7 c). The fitted densities support this attribution but one should bear in mind that water molecules are embedded in PEO in contact with humid air. A rough estimation of a grafting surface density (σ_{PEO}) and of the corresponding mean distance between grafting points (D_{PEO}) can be obtained assuming a dry polymer layer from: $\sigma_{PEO} = h_{PEO}\rho_{PEO}N_A/M_n$ and $D_{PEO} = 2/\sqrt{\pi\sigma_{PEO}}$, where the PEO density was set to ρ_{PEO}~1.1 g/cm^3 and N_A is the Avogadro's number[52-53]. We obtained σ_{PEO} ~2.8 chains/nm² and D_{PEO}~*0.7nm* that corresponds to $\Gamma \sim 4.8 \times 10^{-10}$ mol.cm^{-2}, in perfect agreement with expected para-benzenesulphonyl acid (-Ar-SO_3H) molar surface coverage values. A 25.5nm thick chromium film was also studied before and after functionalization with pure Brij58 (Cr-Ar-SO_2-Brij58, Figure 8). Since the bare electrode is thicker and its air interface is rougher (1.35nm), the so-called "Kiessig" fringes were lost in the reflectivity curve at larger angles, which somehow reduced the resolution one can reach in the depth profile analysis. For these reasons, the data were well fitted in air (Figure 8 a) using a single slab for all the organic material (Ar-SO_2-Brij58). It gave an organic coating thickness of 3.7nm with a roughness of 1.48nm with Cr and 0.43nm on top. The electron density found is thus a mixture of the materials that compose the slab plus water molecules associated to the PEO blocks (Figure 8 b and c).

Gold and metals with a high electron density are commonly used for biosensors (SPR, QCM, EIS, ...). Their high electron density forbids the use of x-ray reflectivity to probe thin organic coating profiles (ρ^e_{Au} ~4.66 e$^-$/ Å^3, so 2.3 times ρ^e_{Cr}). Indeed, the contrast between the coating and air is much lower than the one between gold and other materials, so that the reflectivity signal is dominated by the gold layer features. To illustrate this, we plotted a simulation of the x-ray reflectivity that would correspond to an equivalent sample built on gold instead of chrome (Figure 7 a, dotted and slash lines correspond to the bare and coated gold layer, respectively). The difference between the two gold reflectivity curves (before and after functionalization with –Ar-SO_2-PEO_9CH_3) is negligible compared to the difference we measured on chrome electrodes (red and blue curves). Thus, the use of a relatively low electron density electrode material allowed us to probe the organic monolayer grafted.

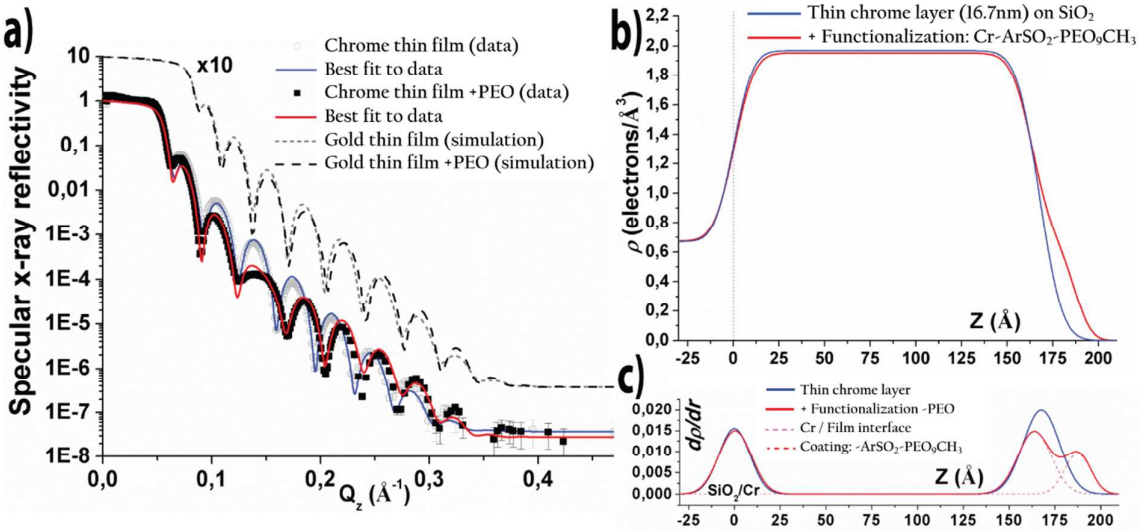

Figure 7. a) Specular x-ray reflectivity data of a 16.7nm bare chromium film (grey dots) and same film functionalized with Ar-SO_2-Brij58 (black dots), with best fits to the data in blue and red, respectively. The dashed and dotted curves correspond respectively to simulations for a bare gold electrode (with same thickness and roughness than Cr) before and after functionalization with the same organic layer, respectively ; b) Electronic density profiles of the best fit to the chromium data; c) the density profile's first derivative.

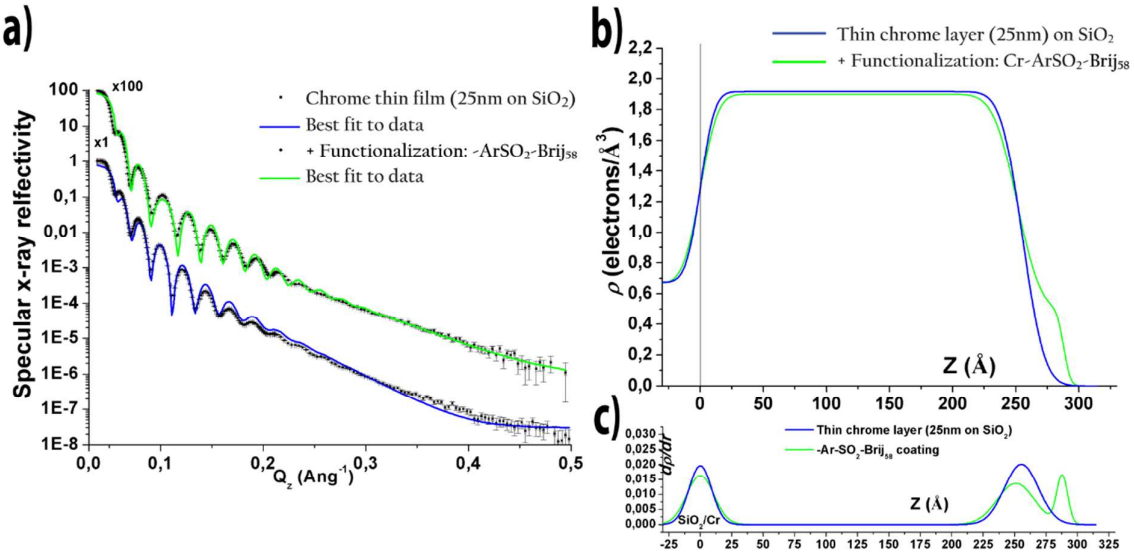

Figure 8. a) Specular X reflectivity of a 25nm sputtered chromium film (blue line) and a Ar-SO2-Brij58 functionalized chromium film (green line) ; b) Electronic density profiles of the same surfaces; c) The density profile's first derivative.

Conclusions.

This paper presents a simple and versatile surface chemistry for any conducting or semiconducting materials based on the covalent grafting of weakly reactive commercial surfactants, which can drastically change their surface properties. We avoided cumbersome organic synthesis steps, since all molecules are commercially available with end-moieties such as –OH, –COOH, -NH_2, etc. The two step functionalization was tested on gold (rough and flat) and chromium films (ultra-flat with sub-nanometer roughness). First, the electrode (M) was pre-functionalized from the reduction of aryldiazonium salts (Ar-SO_3H) that were transformed in a highly reactive M-Ar-SO_2Cl coating. Secondly, surfactant molecules with a hydroxyl terminating (R-OH) were covalently bound by nucleophilic substitution to form an M-Ar-SO_3-R coating. Contrarily to previous approaches developed to graft Brij molecules (on activated alkanethiol SAMs for instance [54]), we did not use thiolates on gold but a C radical linker which is more robust, resistant toward E-field and less hydrophobic. Here, unmodified amphiphilic surfactants such as Brij or CiEj were grafted via their hydrophilic block (anchor). Once grafted, they drastically change the electrodes wettability and their physical properties.

The change of contact angle with water (θ_c) is obviously related to the increasing PEO block length for the Brij and CiEj non-ionic surfactants grafted (Brij58 ($C_{16}H_{33}(OCH_2CH_2)_{20}OH$), Brij52 ($C_{16}H_{33}(OCH_2CH_2)_2OH$), Brij-C10 ($C_{16}H_{33}(OCH_2CH_2)_{10}OH$) and PEO_9-CH_3 ($H(OCH_2)_9CH3$) oligomers). Grafted surfactants then formed an "anchor-harpoon" system with their hydrophobic moiety ready to assemble with analytes hydrophobic groups. Hydrophilic coatings with sparse "anchor-harpoon" molecules were obtained using mixtures of Brij58 and PEO. Adding PEO chains also provides an excellent environment to stabilize a single sparsely tethered bilayer lipid membrane (stBLM). Such electrochemical biosensors are designed to probe biomimetic or biological membranes under electric fields and dynamics of surrounding ions. Specific membrane tethering was demonstrated on these Brij-58/PEO mixed monolayers, following the kinetics of vesicles fusion with SPR and QCM experiments (not shown since the paper focuses on the surface chemistry). In that regard, one should optimize the length of the PEO anchor, the density of anchors and the thickness of the PEO aqueous cushion underneath the tethered membrane, in order to keep a lipid 2D-fluidity that is relevant to biological studies [55].

Different interfacial properties were probed using the electrochemical impedance spectroscopy techniques (EIS in faradaic and non-faradaic modes), and cyclic voltamperometry (CV). We took advantage of our three electrodes setup to study the ions dynamics at the interface with a controlled surface potential and monitored at each step the changes of: ionic double layer capacity; interfacial resistance or charge transfer with Red/Ox probes; .... The designed ultra-flat electrodes are well adapted to surface techniques dedicated to a molecular-scale structural characterization, such as atomic force microscopy. Moreover, the choice of chromium allows one to envision x-ray reflectivity (XRR) experiments to study the thin organic coatings, which would be impossible on gold, silver, platinum,... Reduction of Cr thickness down to 8nm, gave a better resolution of the coating depth profiles obtained from x-rays and gave better optical transparency needed in fluorescent microscopy techniques through the electrode. Combining several investigation methods on the same electrode and avoiding the use of different dedicated substrates or functionalizations for each technique, arouse great interest in the field of biosensors. Tethered proteins or phospholipid membranes on such electrodes further provide a biomimetic model sensor, which constitutes a possible support for biotechnological and medical applications.

ASSOCIATED CONTENT

Supporting information. Gold electrodes cleaning procedure; Grafting kinetics of Brij surfactants in water monitored by QCM; Fit of the EIS data in different representations; X-ray reflectivity measurements of the bare chromium thin films; X-ray photoelectron spectrometry.

AUTHOR INFORMATION

Corresponding Author

*E-mail: guillaume.brotons@univ-lemans.fr. Phone: +33 243832625.

ORCID

Squillace Ophélie (OS): 0000-0003-3840-5065

Brotons Guillaume (GB): 0000-0003-3832-3932

Author Contributions

All authors have given approval to the final version of the manuscript. OS and GB authors contributed equally.

Funding Sources

The French government financially supported this work. All authors declare no competing financial interest. OS received her PhD grant from the French ministry of research and higher education (*via* Ecole Doctorale 3MPL, ED 500).

ACKNOWLEDGMENT

We acknowledge M. Edely for his help in the chromium film preparation (Cr electrodes were performed on the Thin Film Elaboration Platform of IMMM (Université du Maine, Le Mans, France) as well as N.Yaakoubi from ENSIM (Le Mans). We are grateful to A.Bajorek, University of Silesia in Katowice (Poland) who carried out the XPS (X-ray photoelectron spectroscopy) measurements presented in the SI section.

ABBREVIATIONS

Brij58	polyethylen glycol hexadecyle ether $C_{16}H_{33}(OCH_2CH_2)_{20}OH$
AFM	Atomic force microscopy
Ar	aryl
Au	gold
βME	b-mercaptoethanol

Brij52	$C_{16}H_{33}(OCH_2CH_2)_2OH$
Brij-C10	$C_{16}H_{33}(OCH_2CH_2)_{10}OH$
C_Nyquist	Real and Imaginary part of capacitance versus *frequency*
CPE	constant phase element
CPE_{dc}	constant phase element of double layer
CPE_W	constant phase element of Warburg
Cr	chromium
CV	cyclic voltammetry
EIS	electrochemical impedance spectroscopy
FC16	29-Hexadecyloxy-3,6,9,12,15,18,21,24,27,31-decaoxaheptatetracontan-1-thiol
HC18	Z-20-(Z-octadec-9-enyloxy)-3,6,9,12,15,18,22-heptaoxatetracont-31-ene-1-thiol
M	metal
PEG	Polyethylene glycol
PEO	Polyethylene oxide
QCM	quartz crystal microbalance
R	Resistance
R_{ci}	Resistance of counterions
R_{ct}	Resistance of charge transfer
R_S	Resistance of solution
SAM	Self-assembled molecules
SEEC	Surface enhance ellipsometry contrast
SIP	surface initiated polymerization
SPR	surface plasmon resonance
tBLM	tethered bilayer lipid membrane
stBLM	sparsely tethered lipid membranes
WC14	20-tetradecyloxy-3,6,9,12,15,18,22-heptaoxahexatricontane-1-thiol
XPS	*X-ray photoelectron spectrometry*
XRR	x-ray reflectivity
Z_Nyquist	Real and Imaginary part of impedance versus *frequency*

REFERENCES

(1) Milner, S. T. Polymer Brushes. *Science* **1991,** *251*, 905-914.

(2) Kodoyianni, V. Spr Principles. *BioTechniques* **2011,** *50*, 32-40.

(3) Stelzle, M.; Weissmüller, G.; Sackmann, E. On the Application of Supported Bilayers as Receptive Layers for Biosensors with Electrical Detection. *The Journal of Physical Chemistry* **1993,** *97*, 2974-2981.

(4) Okahata, Y.; Ebato, H. Application of a Quartz-Crystal Microbalance for Detection of Phase Transitions in Liquid Crystals and Lipid Multibilayers. *Analytical Chemistry* **1989,** *61*, 2185-2188.

(5) Cooper, M. A. Label-Free Screening of Bio-Molecular Interactions. *Analytical and Bioanalytical Chemistry* **2003,** *377*, 834-842.

(6) Niikura, K.; Matsuno, H.; Okahata, Y. Direct Monitoring of DNA Polymerase Reactions on a Quartz-Crystal Microbalance. *Journal of the American Chemical Society* **1998,** *120*, 8537-8538.

(7) Roussille, L.; Brotons, G.; Ballut, L.; Louarn, G.; Ausserré, D.; Ricard-Blum, S. Surface Characterization and Efficiency of a Matrix-Free and Flat Carboxylated Gold Sensor Chip for Surface Plasmon Resonance (Spr). *Analytical and Bioanalytical Chemistry* **2011,** *401*, 1601-1617.

(8) Ausserré, D.; Khachfe R, A.; Roussille, L.; Brotons, G.; Vonna, L.; Lemarchand, F.; Zerrad, M.; Amra, C. *Anti-Reflecting Absorbing Layers for Electrochemical and Biophotonic Applications* 2014; Vol. 5. p 5.

(9) Love, J. C.; Estroff, L. A.; Kriebel, J. K.; Nuzzo, R. G.; Whitesides, G. M. Self-Assembled Monolayers of Thiolates on Metals as a Form of Nanotechnology. *Chemical Reviews* **2005,** *105*, 1103-1170.

(10) Laibinis, P. E.; Whitesides, G. M.; Allara, D. L.; Tao, Y. T.; Parikh, A. N.; Nuzzo, R. G. Comparison of the Structures and Wetting Properties of Self-Assembled Monolayers of N-Alkanethiols on the Coinage Metal Surfaces, Copper, Silver, and Gold. *Journal of the American Chemical Society* **1991,** *113*, 7152-7167.

(11) Garg, N.; Carrasquillo-Molina, E.; Lee, T. R. Self-Assembled Monolayers Composed of Aromatic Thiols on Gold: Structural Characterization and Thermal Stability in Solution. *Langmuir* **2002,** *18*, 2717-2726.

(12) Delamar, M.; Hitmi, R.; Pinson, J.; Saveant, J. M. Covalent Modification of Carbon Surfaces by Grafting of Functionalized Aryl Radicals Produced from Electrochemical Reduction of Diazonium Salts. *Journal of the American Chemical Society* **1992,** *114*, 5883-5884.

(13) Bélanger, D.; Pinson, J. Electrografting: A Powerful Method for Surface Modification. *Chemical Society Reviews* **2011,** *40*, 3995-4048.

(14) Harper, J. C.; Polsky, R.; Wheeler, D. R.; Brozik, S. M. Maleimide-Activated Aryl Diazonium Salts for Electrode Surface Functionalization with Biological and Redox-Active Molecules. *Langmuir* **2008,** *24*, 2206-2211.

(15) D'Amours, M.; Bélanger, D. Stability of Substituted Phenyl Groups Electrochemically Grafted at Carbon Electrode Surface. *The Journal of Physical Chemistry B* **2003,** *107*, 4811-4817.

(16) Shewchuk, D. M.; McDermott, M. T. Comparison of Diazonium Salt Derived and Thiol Derived Nitrobenzene Layers on Gold. *Langmuir* **2009,** *25*, 4556-4563.

(17) Adenier, A.; Combellas, C.; Kanoufi, F.; Pinson, J.; Podvorica, F. I. Formation of Polyphenylene Films on Metal Electrodes by Electrochemical Reduction of Benzenediazonium Salts. *Chemistry of Materials* **2006,** *18*, 2021-2029.

(18) Adenier, A.; Bernard, M.-C.; Chehimi, M. M.; Cabet-Deliry, E.; Desbat, B.; Fagebaume, O.; Pinson, J.; Podvorica, F. Covalent Modification of Iron Surfaces by Electrochemical Reduction of Aryldiazonium Salts. *Journal of the American Chemical Society* **2001,** *123*, 4541-4549.

(19) Hinge, M.; Gonçalves, E. S.; Pedersen, S. U.; Daasbjerg, K. On the Electrografting of Stainless Steel from Para-Substituted Aryldiazonium Salts and the Thermal Stability of the Grafted Layer. *Surface and Coatings Technology* **2010,** *205*, 820-827.

(20) Bouden, S.; Pinson, J.; Vautrin-Ul, C. Electrografting of Diazonium Salts: A Kinetics Study. *Electrochemistry Communications* **2017,** *81*, 120-123.

(21) Nielsen, L. T.; Vase, K. H.; Dong, M.; Besenbacher, F.; Pedersen, S. U.; Daasbjerg, K. Electrochemical Approach for Constructing a Monolayer of Thiophenolates from Grafted Multilayers of Diaryl Disulfides. *Journal of the American Chemical Society* **2007,** *129*, 1888-1889.

(22) Leroux, Y. R.; Fei, H.; Noël, J.-M.; Roux, C.; Hapiot, P. Efficient Covalent Modification of a Carbon Surface: Use of a Silyl Protecting Group to Form an Active Monolayer. *Journal of the American Chemical Society* **2010,** *132*, 14039-14041.

(23) Combellas, C.; Jiang, D.-e.; Kanoufi, F.; Pinson, J.; Podvorica, F. I. Steric Effects in the Reaction of Aryl Radicals on Surfaces. *Langmuir* **2009,** *25*, 286-293.

(24) Nguyen, V. Q.; Sun, X.; Lafolet, F.; Audibert, J.-F.; Miomandre, F.; Lemercier, G.; Loiseau, F.; Lacroix, J.-C. Unprecedented Self-Organized Monolayer of a Ru(Ii) Complex by Diazonium Electroreduction. *Journal of the American Chemical Society* **2016,** *138*, 9381-9384.

(25) Esnault, C.; Chénais, B.; Casse, N.; Delorme, N.; Louarn, G.; Pilard, J.-F. Electrochemically Modified Carbon and Chromium Surfaces for Afm Imaging of Double-Strand DNA Interaction with Transposase Protein. *ChemPhysChem* **2013,** *14*, 338-345.

(26) Harder, P.; Grunze, M.; Dahint, R.; Whitesides, G. M.; Laibinis, P. E. Molecular Conformation in Oligo(Ethylene Glycol)-Terminated Self-Assembled Monolayers on Gold and Silver Surfaces Determines Their Ability to Resist Protein Adsorption. *The Journal of Physical Chemistry B* **1998,** *102*, 426-436.

(27) Bahr, J. L.; Yang, J.; Kosynkin, D. V.; Bronikowski, M. J.; Smalley, R. E.; Tour, J. M. Functionalization of Carbon Nanotubes by Electrochemical Reduction of Aryl Diazonium Salts: A Bucky Paper Electrode. *Journal of the American Chemical Society* **2001,** *123*, 6536-6542.

(28) Wegnerc, G. Control of Molecular and Supramolecular Architecture of Polymers, Polymersystems and Nanocomposites. *Molecular Crystals and Liquid Crystals Science and Technology. Section A. Molecular Crystals and Liquid Crystals* **1993,** *235*, 1-34.

(29) McCabe, I. P.; Forstner, M. B. Polymer Supported Lipid Bilayers. *Open Journal of Biophysics* **2013,** *Vol.03No.01*, 11.

(30) Wagner, M. L.; Tamm, L. K. Tethered Polymer-Supported Planar Lipid Bilayers for Reconstitution of Integral Membrane Proteins: Silane-Polyethyleneglycol-Lipid as a Cushion and Covalent Linker. *Biophysical Journal* **2000,** *79*, 1400-1414.

(31) Hertrich, S.; Stetter, F.; Ruhm, A.; Hugel, T.; Nickel, B. Highly Hydrated Deformable Polyethylene Glycol-Tethered Lipid Bilayers. *Langmuir* **2014,** *30*, 9442-9447.

(32) Liu; Gooding, J. J. An Interface Comprising Molecular Wires and Poly(Ethylene Glycol) Spacer Units Self-Assembled on Carbon Electrodes for Studies of Protein Electrochemistry. *Langmuir* **2006,** *22*, 7421-7430.
(33) Cao, C.; Zhang, Y.; Jiang, C.; Qi, M.; Liu, G. Advances on Aryldiazonium Salt Chemistry Based Interfacial Fabrication for Sensing Applications. *ACS Applied Materials & Interfaces* **2017,** *9*, 5031-5049.
(34) Mahouche-Chergui, S.; Gam-Derouich, S.; Mangeney, C.; Chehimi, M. M. Aryl Diazonium Salts: A New Class of Coupling Agents for Bonding Polymers, Biomacromolecules and Nanoparticles to Surfaces. *Chemical Society Reviews* **2011,** *40*, 4143-4166.
(35) Chassaing, G. J.; Sigrist, M. L. Étude De La Conductibilité Électrique De Couches Minces De Chrome Préparées Par Évaporation Thermique. Détermination Du Libre Parcours Moyen Et De La Densité Des Électrons De Conduction. *Thin Solid Films* **1973,** *16*, 37-47.
(36) Julkarnain, M.; Hossain, J.; Sharif, K.; Khan, K. Temperature Effect on the Electrical Properties of Chromium Oxide (Cr2o3) Thin Films. *Journal of Optoelectronics and Advanced Materials* **2011,** *13*, 485-490.
(37) Liu, Y.-C.; McCreery, R. L. Reactions of Organic Monolayers on Carbon Surfaces Observed with Unenhanced Raman Spectroscopy. *Journal of the American Chemical Society* **1995,** *117*, 11254-11259.
(38) McGillivray, D. J.; Valincius, G.; Vanderah, D. J.; Febo-Ayala, W.; Woodward, J. T.; Heinrich, F.; Kasianowicz, J. J.; Lösche, M. Molecular-Scale Structural and Functional Characterization of Sparsely Tethered Bilayer Lipid Membranes. *Biointerphases* **2007,** *2*, 21-33.
(39) GABRIELLI, C. Méthodes Électrochimiques: Mesures D'impédances. *Techniques de l'ingénieur. Corrosion vieillissement* **1998**.
(40) Bard, A. J.; Faulkner, L. R. Basic Potential Step Methods. *Electrochemical Methods: Fundamentals and Applications* **2001**, 156-225.
(41) Khoshroo, M.; Rostami, A. A. Eis Study of the Redox Reaction of Fe(Cn)63-/4- at Glassy Carbon Electrode Via Diazonium Reduction in Aqueous and Acetonitrile Solutions. *Journal of Electroanalytical Chemistry* **2008,** *624*, 205-210.
(42) Janek, R. P.; Fawcett, W. R.; Ulman, A. Impedance Spectroscopy of Self-Assembled Monolayers on Au (111): Sodium Ferrocyanide Charge Transfer at Modified Electrodes. *Langmuir* **1998,** *14*, 3011-3018.
(43) Baranton, S.; Bélanger, D. Electrochemical Derivatization of Carbon Surface by Reduction of in Situ Generated Diazonium Cations. *The Journal of Physical Chemistry B* **2005,** *109*, 24401-24410.
(44) Chen, J.; Zhang, J.; Wang, K.; Lin, X.; Huang, L.; Chen, G. Electrochemical Biosensor for Detection of Bcr/Abl Fusion Gene Using Locked Nucleic Acids on 4-Aminobenzenesulfonic Acid-Modified Glassy Carbon Electrode. *Anal Chem* **2008,** *80*, 8028-8034.
(45) Bisquert, J.; Compte, A. Theory of the Electrochemical Impedance of Anomalous Diffusion. *Journal of Electroanalytical Chemistry* **2001,** *499*, 112-120.
(46) Hu, F.; Karweik, D. H.; Kuwana, T. Activation and Deactivation of Glassy Carbon Electrodes. *Journal of electroanalytical chemistry and interfacial electrochemistry* **1985,** *188*, 59-72.
(47) Valincius, G.; Meškauskas, T.; Ivanauskas, F. Electrochemical Impedance Spectroscopy of Tethered Bilayer Membranes. *Langmuir* **2011,** *28*, 977-990.
(48) Wang, H.; Pilon, L. Intrinsic Limitations of Impedance Measurements in Determining Electric Double Layer Capacitances. *Electrochim Acta* **2012,** *63*, 55-63.

(49) Hinge, M.; Ceccato, M.; Kingshott, P.; Besenbacher, F.; Pedersen, S. U.; Daasbjerg, K. Electrochemical Modification of Chromium Surfaces Using 4-Nitro- and 4-Fluorobenzenediazonium Salts. *New Journal of Chemistry* **2009,** *33*, 2405-2408.

(50) Budvytyte, R.; Valincius, G.; Niaura, G.; Voiciuk, V.; Mickevicius, M.; Chapman, H.; Goh, H.-Z.; Shekhar, P.; Heinrich, F.; Shenoy, S.; Lösche, M.; Vanderah, D. J. Structure and Properties of Tethered Bilayer Lipid Membranes with Unsaturated Anchor Molecules. *Langmuir* **2013,** *29*, 8645-8656.

(51) Heinrich, F.; Ng, T.; Vanderah, D. J.; Shekhar, P.; Mihailescu, M.; Nanda, H.; Lösche, M. A New Lipid Anchor for Sparsely Tethered Bilayer Lipid Membranes†. *Langmuir* **2009,** *25*, 4219-4229.

(52) De Gennes, P.-G. *Scaling Concepts in Polymer Physics*; Cornell university press1979.

(53) Sommer, C.; Pedersen, J. S.; Stein, P. C. Apparent Specific Volume Measurements of Poly (Ethylene Oxide), Poly (Butylene Oxide), Poly (Propylene Oxide), and Octadecyl Chains in the Micellar State as a Function of Temperature. *The Journal of Physical Chemistry B* **2004,** *108*, 6242-6249.

(54) Lahiri, J.; Kalal, P.; Frutos, A. G.; Jonas, S. J.; Schaeffler, R. Method for Fabricating Supported Bilayer Lipid Membranes on Gold. *Langmuir* **2000,** *16*, 7805-7810.

(55) Purrucker, O.; Förtig, A.; Jordan, R.; Tanaka, M. Supported Membranes with Well-Defined Polymer Tethers—Incorporation of Cell Receptors. *ChemPhysChem* **2004,** *5*, 327-335.

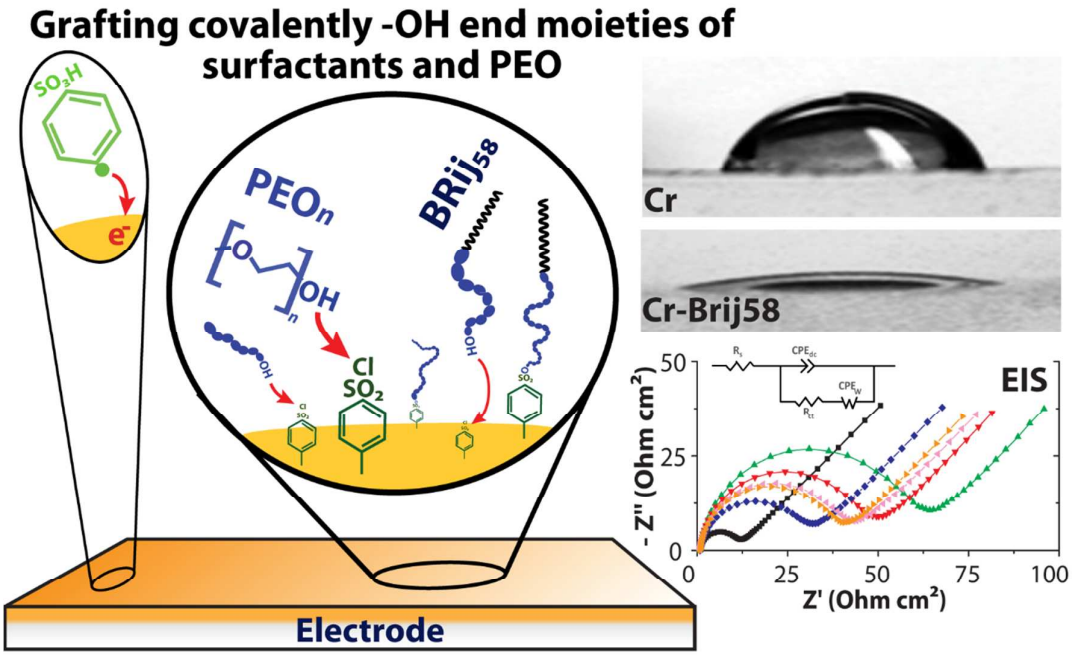

For table of contents (TOC) only